

PAPER

## Particle image reconstruction for particle detection in particle tracking velocimetry

To cite this article: Adam Cheminet *et al* 2018 *Meas. Sci. Technol.* **29** 125202

View the [article online](#) for updates and enhancements.



**IOP | ebooks™**

Bringing you innovative digital publishing with leading voices to create your essential collection of books in STEM research.

Start exploring the **collection** - **download the first chapter of every title for free.**

# Particle image reconstruction for particle detection in particle tracking velocimetry

Adam Cheminet, Jean-François Krawczynski<sup>✉</sup> and Philippe Druault

Sorbonne Université, CNRS, Institut Jean Le Rond d'Alembert, F-75005 Paris, France

E-mail: [jean-francois.krawczynski@sorbonne-universite.fr](mailto:jean-francois.krawczynski@sorbonne-universite.fr)

Received 27 July 2018, revised 12 October 2018

Accepted for publication 19 October 2018

Published 16 November 2018



## Abstract

A new methodology for particle identification and localization in the context of particle tracking velocimetry (PTV) is presented. The aim is to overcome the issue of inherent detection errors under high particle density conditions. The approach is based on the particle position reconstruction through the inversion of a linear model connecting the PTV signal with a particle-based representation of the 3D-to-2D projection. The inversion procedure accounts for both the non-negativity and the sparsity of the sought solution. Simulation tests using synthetically generated images are carried out to evaluate the sensitivity of the proposed method to characteristic parameters such as the particle image density, the particle image size, the model image size, and/or background noise. Its ability to provide better detection performances with higher reliability than conventional techniques is demonstrated.

Keywords: PTV, detection, image reconstruction, sparsity, optimization

(Some figures may appear in colour only in the online journal)

## 1. Introduction

Spatio-temporally resolved velocity measurements techniques based on image analysis are generally classified into two main categories: particle image velocimetry (PIV) and particle tracking velocimetry (PTV). Both rely on seeding particles embedded in a flow field that are made visible within a thin laser sheet and imaged in successive frames separated by a small time interval. PIV essentially tracks features within prescribed regions of the image (interrogation areas). Although it has progressed to a very robust and accurate level, it still suffers from an inherent averaging effect over the area of the interrogation window, which decreases the maximum velocity gradients that can be measured (Scarano 2003, Nogueira *et al* 2005). Therefore, characteristic quantities of small-scale turbulent flows, such as the mean energy dissipation rate, are still challenging to determine from the direct differentiation of the PIV data (Saarenrinne and Piirto 2000, Tanaka and Eaton 2007, Krawczynski *et al* 2010). Inhomogeneous seeding in the vicinity of walls or interfaces also affects the PIV capability to resolve the strong velocity gradients associated with these flow regions (Kahler *et al* 2012). As for PTV, it tracks individual particles and mostly relies on the positional

information of, potentially, a large amount of imaged particles. The velocity field results from a matching procedure between the identified particles in (generally a pair of) successive images. Therefore the smallest resolved scales of the flow depend theoretically only on the mean spacing between particles and the time interval,  $\Delta t$  between frames.

Feng *et al* (2011) identified two kinds of velocity error in PTV. The first kind arises from the particle acceleration, whether due to a change in its speed or its direction, during the time interval between the measurement of its position. This error is unavoidable as long as the motion is unknown, but its amplitude depends on the algorithm used for calculating the displacement from the matched particles. The second kind of error results from uncertainties in the determination of the particle positions. To demonstrate the combined effect of both sources of errors, Feng *et al* (2011) simulated a single particle in a uniform circular motion over a duration of 1000 periods. A random error chosen from a Gaussian distribution was added to the true position to model a measurement error. Their analysis showed that the total velocity error is strongly affected by the particle position uncertainty for small  $\Delta t$ , whereas it is mainly due to the particle acceleration at large  $\Delta t$  only. Undoubtedly, actual flows with strong local

velocity gradients require very small time intervals to be fully characterized. As a consequence, whereas the democratization of the high frame-rate scientific cameras reduces the impact of the unknown motion on the velocity error, the uncertainty in the particle position often becomes the main source of velocity error.

For low seeding densities with homogeneous particle size distributions, the determination of the particle position is trivial because diffraction limited imaging theory indicates that each particle results in a single peak in the image and its intensity distribution can be approximated by a two-dimensional (2D) Gaussian function (Raffel *et al* 2007). Therefore, the particle identification and localization are usually performed after segmentation of the image into meaningful regions followed by a 1D or 2D Gaussian fit applied to the pixels in the vicinity of a local intensity maximum (Cowen and Monismith 1997, Marxen *et al* 2000, Ohmi and Li 2000, Mikheev and Zubtsov 2008, Brady *et al* 2009). The simplest and most commonly utilized method for particle identification is the threshold binarization which consists in grouping adjacent pixels into blobs provided their intensities are above a given threshold value. The dynamic threshold binarization (DTB) method proposed by Ohmi and Li (2000) and modified by Mikheev and Zubtsov (2008) locally adjusts the threshold value until either the mean gray level (Ohmi and Li 2000) or the local maximum intensity (Mikheev and Zubtsov 2008) is less than a preset contrast level. Likewise, the erosion/dilation thresholding (EDT) method (Cardwell *et al* 2011) is based on morphological operations and was purposely designed to protect local maxima. Although DTB and EDT are fast and easy to implement, they are unable to deal with the identification of overlapped particles. Other approaches that strive to find the particle location as the maximum of correlation between a model image of the particle and the original image are to be mentioned (Takehara and Etoh 1999). The cascade correlation method (CCM) proposed by Angarita-Jaimes *et al* (2009) suggests that instead of applying the cross-correlation once with the particle mask image, a cascade of cross-correlation makes the correlation peak narrower, thus decreasing the critical separation distance at which two overlapped particles are resolved. Lei *et al* (2012) further improved the accuracy of the CCM algorithm with the use of a Gaussian surface fit instead of a five-point 2D Gaussian fit to find the sub-pixel peak location.

Whatever the adopted strategy is, when the particle density increases, the individual-particle detection and localization efficiency is decreased due to a higher probability of overlapping particles with possibly different sizes, shapes and brightness levels.

In this paper, we present a 2D particle detection algorithm applicable to high-density particle images. The general idea is to reconstruct particle positions in a discrete approach using an imaging model. This method is derived from the tomographic reconstruction developed for 3D-PIV (Elsinga *et al* 2006) and from the particular approach developed by Champagnat *et al* (2014). It is designed with the aim at (1) minimizing the contribution of the particle localization uncertainty in the error of the velocity field; (2) maximizing the spatial resolution which is of major importance for many applications in

fluid mechanics; and (3) minimizing its sensitivity to the characteristic noise inherent to experimental data. The reliability of this method is evaluated with simulation tests performed on synthetic images with adjustable parameters (particle density, overlap ratio, additive noise).

The paper is organized as follows. First the particle identification-based algorithm is described in section 2. Details about the generation of the synthetic database are given in section 3.1 and the statistical tools used to evaluate the detection and localization performances are presented in section 3.2. The results of the simulations are thoroughly covered in sections 4 and 5.

## 2. The particle image reconstruction (PIR) problem

Recently, the development of the so-called tomographic PIV shifted the velocity measurements towards a 3D framework. The 3D motion of the flow is deduced from the volumetric reconstruction of the particles intensity distribution immersed in the flow of interest (Elsinga *et al* 2006). The essential of the mathematical abstraction behind this technique is the projection model between the 3D space of the seeding particles and the 2D space of their related recorded signal in the multiview images. This projection model is based on a calibration procedure and the physical knowledge of the process. Every model in the literature takes the form of a linear connection between the 3D distribution of the particles and the set of multiview images:

$$\mathbf{Ax} = \mathbf{b}, \quad (1)$$

where  $\mathbf{b}$  gathers the pixels from the multiview images,  $\mathbf{x}$  collects the intensities of the particles within the illuminated volume and the matrix  $\mathbf{A}$  depends on the nature of the projection model. Therefore, the volume reconstruction of the particles distribution results from the inversion problem of a linear system. Two different conceptual representations of the projection model have been adopted to build the matrix  $\mathbf{A}$ . On a historical basis, the tomographic model introduced in the seminal paper (Elsinga *et al* 2006) has been used with success in many contributions of the 3D-PIV community. It assumes that the pixel intensity is the result of an integration process along the light of sight of the particles intensity, spatially distributed in the volume. On the other hand, a physics-driven representation based on the intrinsic properties of the optical system (essentially its aperture diffraction) has been derived to model the image formation (Champagnat *et al* 2014). Interestingly, whereas both models have been designed with the aim at representing the same physical problem, they exhibit some major differences. While the tomographic model approach obtains a smooth blob-reconstruction from the point spread function footprint (PSF) on the 2D images, the particle approach builds a sparse vector indicating the position of a particle within a few voxels and their associated intensities. We propose in this paper to take advantage of this particular feature and set forth a particle image reconstruction approach written in the form of (1). The inversion of the latter seeks the 2D density signal in a sparse space, with the aim of recovering the localizations of particles with, potentially, large overlapping ratios.

We expose below details about the image model based on the concept of point spread function in section 2.1. The specifics of the inversion procedure of the linear problem are discussed in section 2.2. In the last part of this section, further information is given about the implementation of this method and the final localization process (section 2.3).

### 2.1. The PSF model

Assuming  $P$  particles seen as point sources of intensity  $E_p$  and located at  $\mathbf{X}$  in the region of interest, Champagnat *et al* (2014) proposed to model the image intensity  $I$  at a point  $\mathbf{x} \in \mathbb{R}^2$  of the image as

$$I(\mathbf{x}) = \sum_{p=1}^P E_p h_{\mathbf{x}_p}(\mathbf{x} - F(\mathbf{X}_p)), \quad (2)$$

where  $F : \mathbb{R}^3 \rightarrow \mathbb{R}^2$  is the projection operator of a 3D point in the volume onto the image plane and the function  $h : \mathbb{R}^2 \rightarrow \mathbb{R}_+$  is the so-called point spread function (PSF) modeling the formation of the Airy-spots on the image. Therein, the PSF is written as a 2D integrated Gaussian intensity distribution characterized by its standard deviation  $\sigma_{\text{psf}}$ . *This approximation is close to the Airy function given by the Fraunhofer diffraction theory of a monochromatic spot through a circular lens. It is accurate as long as the dimension of the particle in the test section is small compared to the impulse response of the optical system as it is generally the case* (Lecordier *et al* 2004). We note however that the PSF is not restricted to Airy-like functions as it can also take into account, if duly calibrated, defocalisation, astigmatism and other optical effects.

Whereas the tomographic PIV aims at constructing the 3D density signal in a sparse 3D space, the present 2D-PTV approach seeks to determine the particles coordinates in the 2D image with the finest possible accuracy. In practice, the image intensity  $I(\mathbf{x})$  is discretized by the camera sensors onto an array of  $N$  pixels, each denoted  $\mathbf{k} = (k_1, k_2)$ . The idea is to provide a discretized representation of the unknown space which encodes the particles image positions. To this end, a discretized version of (2) can be derived by imposing to  $\mathbf{x}$  and  $\mathbf{X}_p$  to take on values in some discrete sets (Champagnat *et al* 2014):

$$I(\mathbf{k}) \approx \sum_{\mathbf{n}} h(\mathbf{k} - \mathbf{n}\Delta_{\tilde{\mathbf{E}}}) \tilde{\mathbf{E}}(\mathbf{n}), \quad (3)$$

where  $\mathbf{I}$  is the array of image pixels indexed by  $\mathbf{k}$  and  $\tilde{\mathbf{E}}$  is the array which encodes the discrete representation of the unknown space. It is composed of  $M$  sub-pixels each denoted  $\mathbf{n}$  of width  $\Delta_{\tilde{\mathbf{E}}}$ . Equation (3) is then equivalently written in the form of (1):

$$\mathbf{I} = \mathbf{W}\tilde{\mathbf{E}}, \quad (4)$$

where  $\mathbf{W} = h(\mathbf{k} - \mathbf{n}\Delta_{\tilde{\mathbf{E}}})$  is the so-called weight matrix indexed by  $(\mathbf{k}, \mathbf{n})$ .

This approach therefore seeks for local maxima of the reconstructed intensity field  $\tilde{\mathbf{E}}$  in the refined subspace as point-like representations of the particles. It is to be noticed that the accuracy of this method undoubtedly depends on

the size of the sub-pixel  $\Delta_{\tilde{\mathbf{E}}}$ . A perfect inversion process is expected to provide a single illuminated sub-pixel which identifies the position of the center of the particle. The maximum theoretical error in the case of 1:1 sub-pixel aspect ratio is then  $\frac{\sqrt{2}}{2}\Delta_{\tilde{\mathbf{E}}}$ .

### 2.2. Inversion algorithm

The problem to be solved, i.e. the retrieval of the reconstructed intensity  $\tilde{\mathbf{E}}$  out of the available information in  $\mathbf{I}$  is therefore an inversion problem with respect to a fully discrete model. The choice of the inversion strategy to solve equation (4) must be driven by the following considerations. First, the data collected by the camera is characterized by a limited amount of useful information: the projected signal of the particles on the camera plane occupies only a limited fraction of the full size sensor. Moreover, the collected signal is likely to be corrupted by different types of noises. Hence, the sought particles positions  $\mathbf{n}$  and the collected observations  $I(\mathbf{k})$  may actually not match perfectly the linear model (1). Second, the construction of the weight matrix  $\mathbf{W}$  on a refined sub-space leads us to deal with an under-determined problem of a very high dimensionality:  $\mathbf{W}$  is a *short and fat* matrix which has much more columns than rows ( $M \gg N$ ). As a consequence, the problem to be solved has theoretically an infinite number of solutions. One must therefore resort to some known information on the physical perspective in order to single out a proper solution as, for example, the fact that the underlying parameters represent quantities that can only take on non-negative values since the reconstructed field encodes the intensities  $\tilde{\mathbf{E}}$  in equation (4). Ideally, the sought solution is also expected to be very sparse. We then want to capitalize on these requirements and use an inversion algorithm which is well adapted to recover a sparse non-negative solution. Among the popular methods to produce an estimate for  $\tilde{\mathbf{E}}$ , we single out the very popular *non-negative least square* (NNLS). We thus consider the following optimization problem:

$$\text{minimize } \frac{1}{2} \|\mathbf{W}\tilde{\mathbf{E}} - \mathbf{I}\|_2, \mathbf{W} \in \mathbb{R}^{N \times M}, \mathbf{I} \in \mathbb{R}^N \text{ subject to } \tilde{\mathbf{E}} \geq 0, \quad (5)$$

where  $N$  is the number of pixels in the original image and  $M$  is the number of sub-pixels in the reconstruction field. The algorithm of this minimization problem is directly implemented in Matlab as the function *lsqnonneg*. It executes the active-set algorithm of Lawson *et al* (1974). Although it is a *greedy* algorithm in terms of computing time and resources when confronted to large scale problems, we will show with various simulation tests that its implementation within our methodology is well suited to sparse recovery. Moreover, the sequentialization of its implementation is proposed in section 5. It is shown to perform with significant computing time savings when large scale problems are considered.

We also acknowledge many others methods proposed in the literature to solve equation (4), in particular in the context of the volumetric reconstruction of the particles distribution. Among the family of the '*row-action methods*', the '*algebraic reconstruction technique*' (ART) (Petra *et al* 2007), '*the*



multiplicative algebraic reconstruction technique' (MART) (Elsinga *et al* 2006), and the 'simultaneous multiplicative algebraic reconstruction technique' (SMART) (Atkinson and Soria 2009) were advocated to build a tomographic PIV solution.

### 2.3. Implementation

Most of the approaches dedicated to particle detection and localization in PTV first proceed with a segmentation of the particle image. This step is crucial as it acts as a problem size reduction and it provides the algorithm with an initial solution. The aim is to select the minimum amount of pixels and to separate the useful signal, i.e. the discretization of the particle image, from the noise corruption. The simplest and most usual method for grouping adjacent pixels into particles-containing blobs is the threshold binarization. However, such a procedure is expected to crucially impact the following steps of the proposed method herein. Since our reconstruction problem (4) is ill-posed, the solution is very sensitive to the initial solution and more specifically on the set of unknowns. We rather choose to proceed without any pixel selection, except those of non-null intensities. Consequently, the built weight matrix  $W$  is of  $\tilde{N} \times \tilde{M}$  extend, with potentially  $\tilde{N} < N$  and  $\tilde{M} < M$ . The particular case  $\tilde{N} = N$  and  $\tilde{M} = M$  is likely to be obtained when noisy images with large particle densities are considered.

The reader is warned here of the notation convention in this paper. Although the PSF model is used in both the particle images generation and the weight matrix construction, the size parameter used in the former case is termed as  $\sigma_{\text{psf}}$  whereas it is referred as  $\sigma_{\text{recon}}$  in the latter case. Unless otherwise specified,  $\sigma_{\text{recon}} = \sigma_{\text{psf}}$ .

Once the reconstructed intensity field  $\tilde{E}$  in the refined subspace is obtained from the inversion of the linear system, point-like representations of the particles are determined as local maxima of the sub-image. This is performed using a morphological operation (dilation) with a square structuring element of width  $L_{\text{sq}}$ . The determination of the optimal size of the structuring element is specifically discussed in sections 4.2 and 4.4.

The code of our detection algorithm, denoted  $\text{PIR}_{\text{NNLS}}$  in the rest of the paper, is implemented in Matlab and makes use of its high vectorization level and its optimized built-in functions. An other version of the algorithm, hereafter called  $\text{PIR}_{\text{SMART}}$  uses SMART for the inversion procedure. Results obtained by both versions are compared in sections 4.1 and 4.2.

### 3. Synthetic images and performance metrics

A series of simulation tests are designed to evaluate the performance and robustness of the proposed method against a variety of characteristic parameters. Although we keep in mind that simulations can not fully mimic realistic experimental conditions, the interest of using synthetic images is manifest: (1) the full control of all the parameters involved in the generation of the particle images; (2) the knowledge

of the exact position of the particles enables the characterization of the influence of every single parameter onto the overall algorithm performance; and (3) a comparison of the results given by the proposed algorithm with those by other referenced methods in a well defined framework.

#### 3.1. Synthetic set-up

We consider a volume of uniform illumination seeded with monodisperse particles of diameter  $d_p = 1 \mu\text{m}$  placed at random positions. The camera, with a focal length of 200 mm, is positioned at 1 m along the orthogonal direction of the laser sheet plane. The magnification is thus equal to 0.2. The pixel-size is set to  $20 \mu\text{m}$ . A pin-hole model is assumed (without Scheimpflug adapter for simplicity). The images of particles are synthesized according to equation (2) with the PSF function  $h$  defined by

$$h(x, y) = \frac{1}{4} \left( \text{erf} \left( \frac{x + 0.5}{\sqrt{2}\sigma_{\text{psf}}} \right) - \text{erf} \left( \frac{x - 0.5}{\sqrt{2}\sigma_{\text{psf}}} \right) \right) \times \left( \text{erf} \left( \frac{y + 0.5}{\sqrt{2}\sigma_{\text{psf}}} \right) - \text{erf} \left( \frac{y - 0.5}{\sqrt{2}\sigma_{\text{psf}}} \right) \right), \quad (6)$$

where the width of the 2D Gaussian intensity distribution is defined by its standard deviation  $\sigma_{\text{psf}}$  averaged on the pixel surface, assuming a 100% fill factor. The images generated are single exposure snapshots of  $32 \times 32$  pixel at 8-bit grayscale. The maximum intensity  $I_0$  of the scattered light is assumed to be a function of the depth position  $z$  of the particle in the laser sheet only:

$$I_0 = 255 \exp \left( -\frac{z^2}{\sigma_{\text{laser}}^2} \right), \quad (7)$$

where  $2\sigma_{\text{laser}}$  is the laser sheet thickness, set to 1 mm herein. Model (6) hence considers the particles as independent scattering sites and the intensity level of every pixel on the camera sensor results from the summation of all the associated particles contributions.

A cautionary remark to be addressed here concerns the speckle limit which is never reached in this study. The speckle phenomena is likely to occur when the source density defined as the average number of imaged particles multiplied by the squared equivalent diameter of the particle image exceeds one (Adrian 1984). For the specific test reported in section 4.4, the largest generated  $N_{\text{ppp}}$  of about 0.11 multiplied by the average area of the equivalent 2.4 pixel diameter (the factor  $\pi/4$  is actually omitted in the definition of Adrian (1984)) results in a ratio of 45% of the particles image overlap. This upper boundary remains below the speckle limit.

Otherwise, a Gaussian distribution representing camera noise can be added to the particle images (see section 4.5 for further details).

#### 3.2. Performance metrics

The performance of our detection method is quantified in this paper by two metrics suggested by Ruhnau *et al* (2005): the

yield and the reliability, both defined hereafter. A detection is called a true positive (TP) if it satisfies two conditions: (1) it is in the neighborhood of a particle and, (2) it is the nearest detection to this particle. While the former condition requires to arbitrarily define a neighborhood radius of tolerance, the latter one ensures that a TP is associated with only one particle. In every simulation test discussed in this paper, the tolerance radius is set to 0.5 pixel. A detection is considered as a false positive (FP), if it is not in the neighborhood of any particle or, if inside the neighborhood of a particle it is not the nearest detection to the particle. Finally, a particle is termed as false negative (FN) if there is no detection in its neighborhood. These criteria enable to define the two metrics as

$$\text{Yield} = \frac{\#TP}{\#TP + \#FN}, \quad \text{Reliability} = \frac{\#TP}{\#TP + \#FP} \quad (8)$$

where #TP, #FP and #FN are the number of TP, FP and FN respectively. Therefore, the yield is the fraction of true detections relative to the amount of generated particles, and the reliability is the fraction of true detections among all detections.

The accuracy of the detections considered as TP is further quantified with the computation of the mean localization error:

$$\text{Error} = \frac{1}{\#TP} \sum_{i=1}^{N_{TP}} \|\mathbf{x}_{TP_i} - \mathbf{x}_{P_i}\|, \quad (9)$$

where  $TP_i$  is the TP associated with the  $i$ th particle  $P_i$ , and  $\mathbf{x}$  is their position in the image. This metric represents the actual distance between the TP position and the exact localization of its associated particle.

#### 4. Numerical tests: particle detections

Let us now attempt to assess the robustness of our method to detect particles within representative experimental conditions. To this end, numerical tests are performed on synthetic images and most of the forward analysis relies on the evaluation of the performance metrics described in section 3.2.

Remember that the accuracy of the detection method discussed throughout this paper is expected to specifically depend on the projection model, its underlying size parameter  $\sigma_{\text{psf}}$ , and on the grid resolution. The first simulation test (see section 4.1) involves the reconstruction of a single simulated particle. It is designed with the aim of setting the optimal grid size,  $\Delta_{\tilde{E}}$ . It is also expected to give insights on the sparsity of the reconstructed field. To this end, the solutions obtained by  $\text{PIR}_{\text{NNLS}}$  and  $\text{PIR}_{\text{SMART}}$  are compared. Section 4.2 then surveys the ability to detect two identical particles when their separation distance is small enough to be considered as critical for most classical detection methods. In section 4.3, simulation tests that involve again the reconstruction of a single simulated particle are carried out to investigate the sensitivity of the detection to a non-perfect knowledge of the PSF size, i.e. when the PSF calibration is either impossible or inaccurate. Finally, more realistic experimental conditions are obtained with sets of synthetic images of varying particle density and

additive noise contribution. The robustness of  $\text{PIR}_{\text{NNLS}}$  with respect to these parameters is evaluated in sections 4.4 and 4.5 respectively.

##### 4.1. Selection of the sub-pixel size $\Delta_{\tilde{E}}$

The accuracy of the solution is expected to strongly depend on  $\Delta_{\tilde{E}}$  (see section 2.1): theoretically the smaller it is, the more accurate the approximation is. However, it is to be kept in mind that the weight matrix,  $W$  to be inverted grows proportionally to  $(1/\Delta_{\tilde{E}})^2$ , as does probably the computational expense. A test is then designed with the aim of selecting a subgrid size,  $\Delta_{\tilde{E}}$  as an optimum between the finest accuracy of the reconstruction and an affordable computational time.

Simulations involving the reconstruction of a single particle are performed. A particle is randomly placed in a  $32 \times 32$  pixel image. We impose the particle to be fully discretized within the image area, i.e. any truncation effect is not studied here. The reliability of the reconstruction is evaluated against PSF standard deviations ranging from  $\sigma_{\text{psf}} = 0.2$  to 1.2. Let us suppose that these values are known *a priori* (from a calibration procedure for example) and the weight matrix is build with  $\sigma_{\text{recon}} = \sigma_{\text{psf}}$ . For each set, 200 images are generated to ensure good convergence of the performance metrics discussed below.

Figure 1 shows the relationship between the localization error of the detected particle and the subgrid size,  $\Delta_{\tilde{E}}$  of the reconstruction space, as obtained by  $\text{PIR}_{\text{NNLS}}$  and  $\text{PIR}_{\text{SMART}}$  for  $\sigma_{\text{psf}} = 0.4$  (figure 1(a)) and  $\sigma_{\text{psf}} = 0.8$  (figure 1(c)). The two inversion algorithms implemented in our method present comparable evolutions over the tested grid sizes. It is observed that the localization error is always below the theoretical maximum error,  $\frac{\sqrt{2}}{2}\Delta_{\tilde{E}}$ .

In order to further discriminate between both inversion algorithms, we choose to represent the evolution of the sparsity of the reconstruction field,  $\tilde{E}$  as a function of  $\Delta_{\tilde{E}}$  for the same tested conditions, see figures 1(b) and (d). The sparsity is classically defined as the ratio of the amount of null-elements of  $\tilde{E}$  to its total number of elements. In an ideal case, only one sub-pixel of the reconstruction field would be non-zero. Clearly, the reconstruction field obtained by  $\text{PIR}_{\text{NNLS}}$  presents a higher level of sparsity than  $\text{PIR}_{\text{SMART}}$ , whatever the sub-grid size. Note that the largest sparsity value obtained with  $\text{PIR}_{\text{NNLS}}$  is actually 0.9998 for  $\Delta_{\tilde{E}} = 1/50$ . This means that eight sub-pixels of the reconstruction field belong to the solution sub-set.

As a preliminary conclusion, this test validates not only the linear model as depicted in equation (4) but also the ability of the reconstruction procedure to recover the particle position with a high level of accuracy. Meanwhile, we set for the rest of this paper the  $\Delta_{\tilde{E}}$  value to 1/20. Refining further down the sub-image grid-size would require a tremendous increase in memory with a negligible gain in the precision of the localization (see figures 1(a) and (c)). Moreover, the sparsity of the reconstruction field being promising, the reconstruction of two closely separated particles is now considered in the following section.

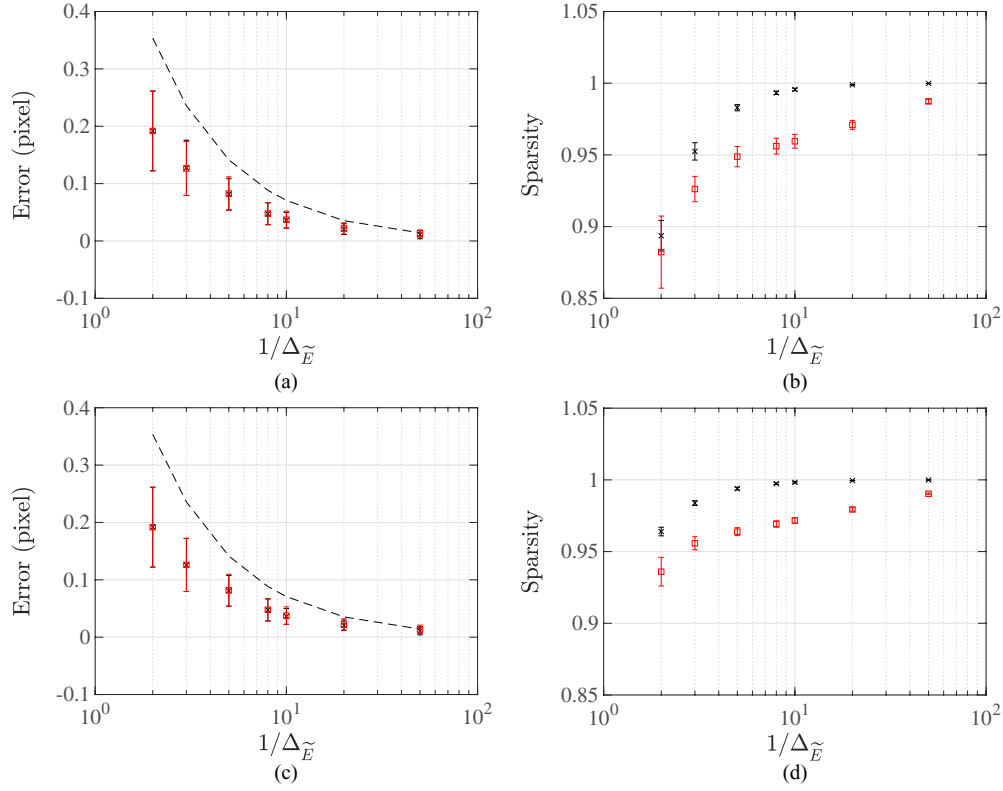


**Figure 1.** Robustness of  $\text{PIR}_{\text{NNLS}}$  (x) and  $\text{PIR}_{\text{SMART}}$  (□) to the reconstruction of a single particle. (a) and (c) Localization error of the detected particle as a function of the sub-pixel size,  $\Delta_{\tilde{E}}$ . Dashed line corresponds to the theoretical maximum error. (b) and (d) Sparsity of the reconstructed field,  $\tilde{E}$  as a function of the sub-pixel size,  $\Delta_{\tilde{E}}$ . (a) and (b)  $\sigma_{\text{psf}} = 0.4$ ; (c) and (d)  $\sigma_{\text{psf}} = 0.8$ .

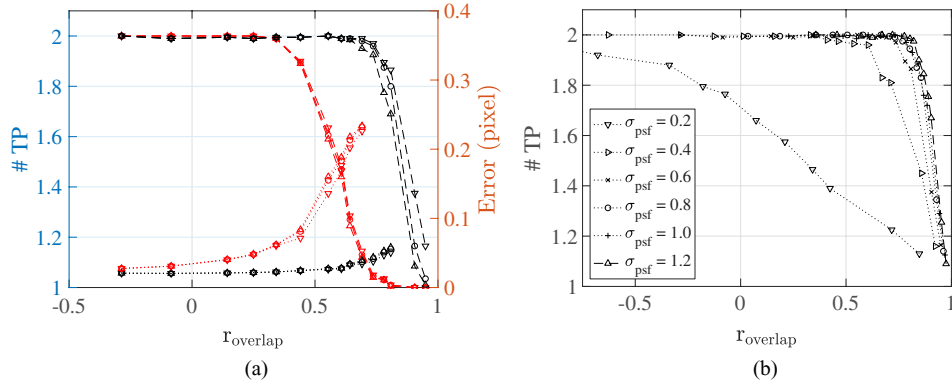


**Figure 2.** (a) #TP (dashed line, left y-axis) and localization error (dotted line, right y-axis) obtained by  $\text{PIR}_{\text{NNLS}}$  (black) and  $\text{PIR}_{\text{SMART}}$  (red) for  $\sigma_{\text{psf}} = 0.6$  as a function of the particle overlap ratio and for three different sizes of square structuring element: ( $\nabla$ ):  $L_{\text{sq}} = 3$  pixels; ( $\circ$ ):  $L_{\text{sq}} = 7$  pixels; ( $\triangle$ ):  $L_{\text{sq}} = 11$  pixels. (b) TP obtained by  $\text{PIR}_{\text{NNLS}}$  for different  $\sigma_{\text{psf}}$  as a function of the particle overlap ratio.

#### 4.2. Overlap test

In order to understand the benefits of our method in distinguishing between two particles in overlapping conditions, simulation tests are performed on images of two identical particles with different separation distance,  $L$ . The detection accuracy is expected to be a function of both  $L$  and the particle image size, as characterized by its diameter,  $D$  with  $D \approx 4 \times \sigma_{\text{psf}}$ . To evaluate the interconnected influence of both  $D$  and  $L$  on the results, the following non-dimensional overlap ratio  $r_{\text{overlap}}$  (Lei et al 2012) is used:

$$r_{\text{overlap}} = \frac{D - L}{D}. \quad (10)$$

For every separation distance  $L$ , 200 images are generated to ensure good statistical convergence of the performance metrics discussed below. The particles are generated following the method described in section 3.1 and randomly distributed in the image. The particle diameter varies from  $D = 0.8$  pixels to  $D = 4.8$  pixels.

Figure 2(a) shows the detection performance metric TP as well as the localization error obtained by  $\text{PIR}_{\text{NNLS}}$  and  $\text{PIR}_{\text{SMART}}$ , as a function of the overlap ratio. It is to be mentioned that the localization error is only computed when two detections are qualified as TP and when at least 50 particle couples are detected. We choose to highlight the results for  $\sigma_{\text{psf}} = 0.6$  but similar trends are observed, whatever the values

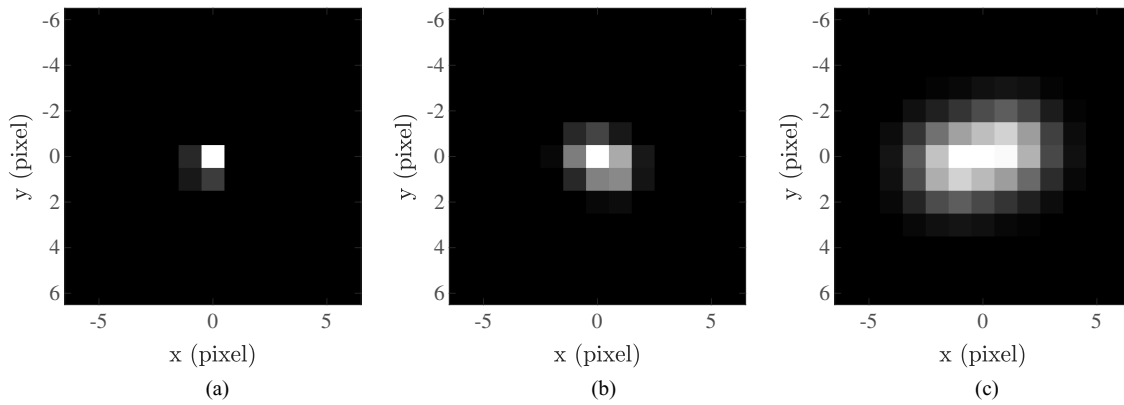


**Figure 3.** Typical synthetic images of two overlapping particles with  $r_{\text{overlap}} = 0.5$ . (a)  $\sigma_{\text{psf}} = 0.2$ ; (b)  $\sigma_{\text{psf}} = 0.6$ ; (c)  $\sigma_{\text{psf}} = 1.4$ .

of the tested  $\sigma_{\text{psf}}$  are. The influence of the size of the structuring element (parametrized as  $L_{\text{sq}}$ , see section 2.3) on the detection performance is also investigated. However, similar trends are obtained for the three tested sizes,  $L_{\text{sq}} = 3, 7$  and  $11$  pixels. Hence, the optimized size of structuring element can not be determined at this stage. Nevertheless,  $L_{\text{sq}}$  is set to  $7$  in the forthcoming tests. Justifications for this choice are given in section 4.4.

The observations to formulate here are illustrative of the encountered difficulties that any detection method has to face when large particle densities are considered: the overlapping issue becomes predominant and the ability to recover with a high level of confidence the localization of two overlapped particles drops down as their separation distance approaches zero, respectively when  $r_{\text{overlap}}$  approaches  $1$ .

Meanwhile, we can further discriminate between the two inversion algorithms implemented in our method. As a consequence of the large sparsity of its reconstructed fields as advocated in section 4.1,  $\text{PIR}_{\text{NNLS}}$  recovers the particle couples with a 100% success rate up to larger overlap ratios than  $\text{PIR}_{\text{SMART}}$  with, additionally, systematic smaller localization errors. For example, two identical particles of diameter  $D = 2.4$  pixel are detected with a 100% success rate, an overlap ratio of  $0.6$  and a localization error within  $0.03$  pixels by  $\text{PIR}_{\text{NNLS}}$  whereas the same performance is obtained by  $\text{PIR}_{\text{SMART}}$  for overlap ratios inferior to  $0.4$  at the cost of larger localization errors. Overall, the averaged errors of  $\text{PIR}_{\text{NNLS}}$  remain within  $0.1$  pixels for overlap ratios up to  $0.8$ . Therefore, these simulation tests clearly show that  $\text{PIR}_{\text{NNLS}}$  is better prone to detect two overlapping particles than  $\text{PIR}_{\text{SMART}}$ . Consequently,  $\text{PIR}_{\text{NNLS}}$  is retained as the inversion algorithm of our method in the rest of this study.

To further illustrate the robustness of  $\text{PIR}_{\text{NNLS}}$  to recover two overlapping particles, the detection metric  $\#TP$  is depicted in figure 2(b) as a function of the overlap ratio and for  $\sigma_{\text{psf}}$  ranging from  $\sigma_{\text{psf}} = 0.2$  to  $\sigma_{\text{psf}} = 1.2$ , i.e. for imaged particle diameter ranging from about  $D = 0.8$  pixels to  $D = 4.8$  pixels. The limitations of this (as well as any other) method are emphasized for small  $\sigma_{\text{psf}}$  values, typically when  $\sigma_{\text{psf}} < 0.4$ . For these conditions,  $\text{PIR}_{\text{NNLS}}$  fails to recover the two particles, even at small overlap ratios. This is intrinsically related to the discretization of the simulated particle on

the synthesized image. As an illustration, couples of simulated particles with different sizes ( $\sigma_{\text{psf}} = 0.2$ ,  $\sigma_{\text{psf}} = 0.6$  and  $\sigma_{\text{psf}} = 1.4$ ) are presented in figure 3 with the same overlap ratio,  $r_{\text{overlap}} = 0.5$ . For  $\sigma_{\text{psf}} = 0.2$ , the complete discretization of the PSF of the overlapping particles is performed on almost one single pixel. This prevents any method from the ability to recover their localizations. On the other hand, at large  $\sigma_{\text{psf}}$  values, the two overlapping particles are clearly discernible. Therefore, the overlap ratio can not be used alone as the objective criterion to discriminate between different detection methods, especially when the simulations are performed on database of significantly different particle image sizes.

#### 4.3. Effect of inaccurate knowledge of $\sigma_{\text{psf}}$

Our inversion method requires an imaging model, designed in our case as an integrated Gaussian function (see equation (6)) of which  $\sigma_{\text{psf}}$  is the only input parameter to be *a priori* determined. An adapted calibration procedure using a particle least-square fitting of a Gaussian PSF template is recommended to obtain an evaluation of this unknown parameter (Schanz et al 2013). Other kinds of calibration exist, such as the slanted-edge method of Reichenbach et al (1991) or more recently, a technique using a collimated light source on a convex spherical mirror (Jemec et al 2017). Whatever is the adopted calibration methodology, residual errors undoubtedly arise. The main source of errors comes from the approximation of the PSF imaging model itself which fails to accurately represent the actual light distribution on the camera CCD of every single particle, with potentially varying sizes or positions in the depth of the laser sheet volume. The purpose of this section is to test the robustness of our method to a non-perfect knowledge of the PSF size. To this end, sets of 200 synthetic  $32 \times 32$  pixel images of a single particle with different  $\sigma_{\text{psf}}$  values are generated.

As a first step, we consider the following test case: the PSF used for the particle image generation is set to  $\sigma_{\text{psf}} = 0.6$ , while the robustness of the detection algorithm is tested against variations of  $\sigma_{\text{recon}}$  in the range  $0.4 \leq \sigma_{\text{recon}} \leq 1$ . Both the yield and the reliability metrics are depicted on figure 4. Clearly, for large  $\sigma_{\text{recon}}$  values with respect to  $\sigma_{\text{psf}}$ , the ability of our method to recover the particles localizations drops down.



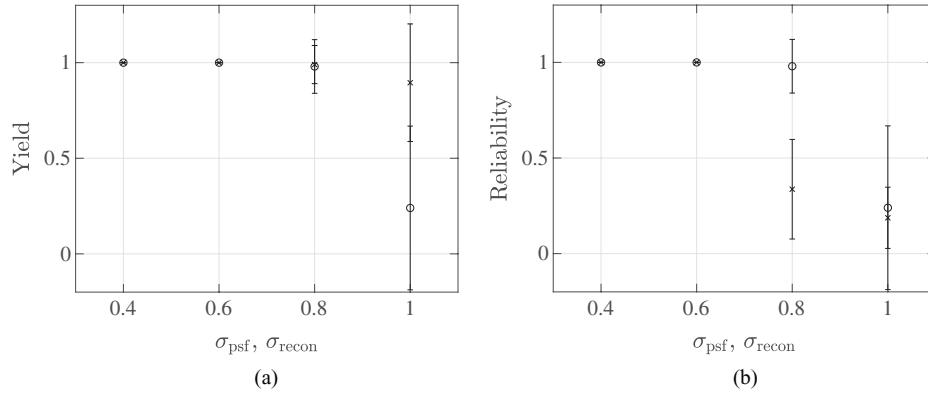


**Figure 4.** Yield (left) and reliability (right) factors as obtained by  $\text{PIR}_{\text{NNLS}}$ . (x):  $\sigma_{\text{psf}}$  values are ranging from 0.4 and 1,  $\sigma_{\text{recon}}$  value is set to 0.6; (o):  $\sigma_{\text{recon}}$  values are ranging from 0.4 and 1,  $\sigma_{\text{psf}}$  value is set to 0.6.

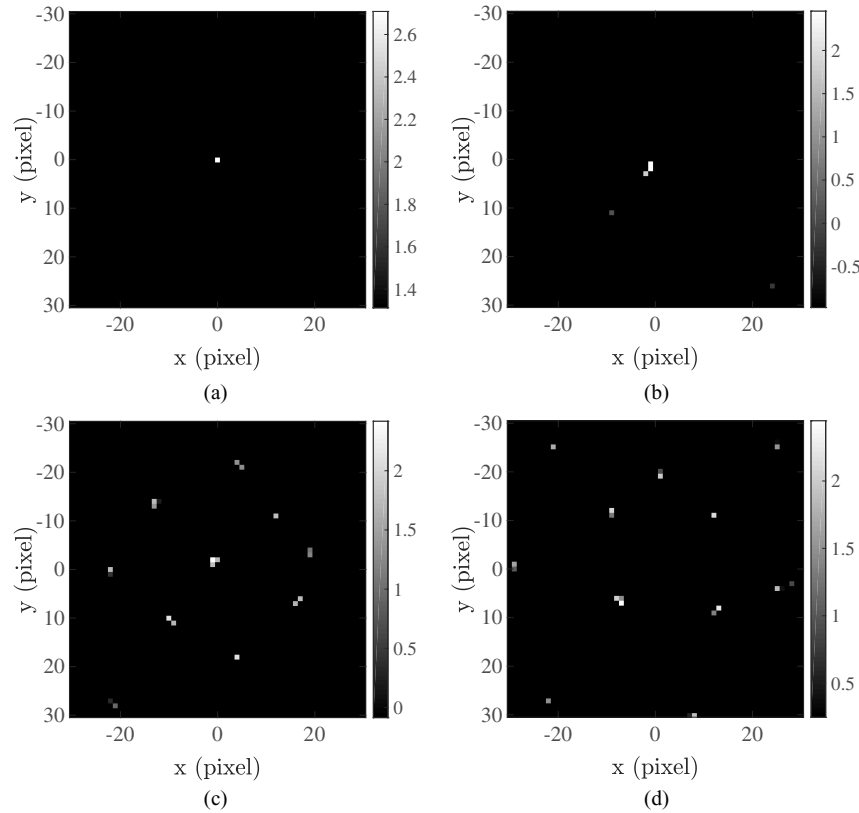


**Figure 5.** Typical intensity distribution in  $\log_{10}$  of the reconstruction field obtained by  $\text{PIR}_{\text{NNLS}}$  for one single particle with  $\sigma_{\text{recon}} = 0.6$ . (a)  $\sigma_{\text{psf}} = 0.4$ ; (b)  $\sigma_{\text{psf}} = 0.6$ ; (c)  $\sigma_{\text{psf}} = 0.8$ ; (d)  $\sigma_{\text{psf}} = 1$ .

However, it is to be emphasized that satisfactory results are obtained with errors on the estimated  $\sigma_{\text{recon}}$  of about 30%.

As a second step, we consider the reversed problem: particle images are generated with  $\sigma_{\text{psf}}$  values ranging from  $\sigma_{\text{psf}} = 0.4$  to  $\sigma_{\text{psf}} = 1$  while the PSF width of the reconstruction model is kept constant, with  $\sigma_{\text{recon}} = 0.6$ . Similar observations can be made: when the  $\sigma_{\text{recon}}$  value is under-estimated with regards to the  $\sigma_{\text{psf}}$  value of the particles, the ability of our method to recover the particles localization is at fault. This particular observation is illustrated with typical reconstruction images of one single particle with different  $\sigma_{\text{psf}}$ , see figure 5. For small  $\sigma_{\text{psf}}$ , i.e.  $\sigma_{\text{psf}} < \sigma_{\text{recon}}$ , the reconstruction field is very sparse: no more than 3 sub-pixels are non-null which

makes the final localization process of the particle easy. For  $\sigma_{\text{psf}} = 0.8$ , i.e. for slightly under-estimated values of  $\sigma_{\text{recon}}$ , the sparsity of the reconstruction is decreased and because the value of the square structuring element,  $L_{\text{sq}}$  is to be kept as small as possible, many FP detections are obtained from this reconstruction image. However, the central sub-pixel corresponding to the localization of the simulated particles is still non-null and a TP detection is also obtained from this image. For  $\sigma_{\text{psf}} = 1$ , i.e. for particle area of about  $4 \times 4$  pixel whereas the estimated particle area as set by  $\sigma_{\text{recon}}$  is about  $2.4 \times 2.4$  pixel, many non-null sub-pixels, dispersed on a large area, are obtained from the inversion procedure. Moreover, the central sub-pixel is no longer part of the solution sub-set.

**Table 1.** Mean performance metrics (reliability and yield) computed with  $\text{PIR}_{\text{NNLS}}$  using three different sizes for the square structuring element.

$N_{\text{ppp}}$	0.021	0.033	0.042	0.053	0.066	0.073	0.087	0.094	0.105
Yield— $L_{\text{sq}} = 3$	0.993	0.990	0.986	0.979	0.976	0.973	0.961	0.957	0.955
Yield— $L_{\text{sq}} = 7$	0.991	0.989	0.984	0.975	0.971	0.970	0.956	0.952	0.951
Yield— $L_{\text{sq}} = 11$	0.992	0.987	0.983	0.973	0.960	0.966	0.955	0.946	0.942
Reliability— $L_{\text{sq}} = 3$	0.939	0.917	0.913	0.899	0.910	0.894	0.876	0.879	0.883
Reliability— $L_{\text{sq}} = 7$	0.983	0.987	0.975	0.973	0.975	0.970	0.956	0.967	0.964
Reliability— $L_{\text{sq}} = 11$	0.988	0.992	0.983	0.979	0.976	0.968	0.964	0.962	0.963

This trend towards a large dispersion of the solution sub-set is an intrinsic characteristic of the optimization (5) when  $\sigma_{\text{recon}} \ll \sigma_{\text{psf}}$ , i.e. when the calibration procedure underestimates the size of the particle images to reconstruct. This can be understood by the fact that the inversion procedure attempts to reconstruct a particle image of large area using particle(s) of small image area(s). Because the imaging model makes use of a summation of particles images, the algorithm artificially creates particles of which the summation of their signal intensities correspond (in the least square sense) to the signal intensity distribution of the large particle.

#### 4.4. Effect of particle density $N_{\text{ppp}}$

Particle image density ( $N_{\text{ppp}}$ ) is a major limiting factor for PTV reliability since large density inhibits an optimized particle identification and localization. In the simulations of this test, the particle image density is varied from  $N_{\text{ppp}} \approx 0.02$  to  $N_{\text{ppp}} \approx 0.11$ . The mean size of the particles is set constant, with  $\sigma_{\text{psf}} = 0.6$ . To ensure statistical convergence of the results discussed below, sets of 30 synthetic  $32 \times 32$  pixel images are generated for every  $N_{\text{ppp}}$ .

Prior to the analysis of the results of this simulation test, we want to definitively state the optimal (if any) size of the square structuring element,  $L_{\text{sq}}$ . Remember that a small value of  $L_{\text{sq}}$  is likely to favor a fine spatial resolution of the detections field. It is also likely to favor a possibly large amount of False Positives, as evidenced on the reconstruction maps of figure 5(c): smaller values than  $L_{\text{sq}} \approx 10$  would not suppress the illuminated pixels located around the true central position from the solution sub-set.

Three different sizes are tested:  $L_{\text{sq}} = 3, 7$  and  $11$  (sub-pixels (to be compared with the size of the discretized pixel which is set to  $1/\Delta_{\tilde{E}} = 20$  as suggested in section 4.1). The mean performance metrics as reported in table 1 exhibit quasi-similar behavior although  $L_{\text{sq}} = 7$  leads to some slightly better results than those computed with  $L_{\text{sq}} = 3$  in term of reliability and those computed with  $L_{\text{sq}} = 11$  in term of yield. Consequently, for the rest of the paper, the final detection step on the reconstruction maps is performed with  $L_{\text{sq}} = 7$ .

We now turn our analysis towards the sensitivity of the  $\text{PIR}_{\text{NNLS}}$  method to the particle density,  $N_{\text{ppp}}$ . For this specific test, the performances of  $\text{PIR}_{\text{NNLS}}$  are compared to the consolidated and widely used dynamic threshold binarization (Ohmi and Li 2000) and to the modified cascade correlation method (Lei et al 2012) hereafter referred as DTB and CCM respectively.

A qualitative illustration of the detected localizations as obtained with the three methods is represented in figure 6 (top row). The same synthetic  $32 \times 32$  pixel image is considered with 104 generated particles, i.e.  $N_{\text{ppp}} = 0.102$ . For this particular case, the performance metrics of the three methods are:  $\text{TP}_{\text{DTB}} = 53$ ,  $\text{TP}_{\text{CCM}} = 45$  and  $\text{TP}_{\text{PIR}_{\text{NNLS}}} = 103$ ;  $\text{FP}_{\text{DTB}} = 12$ ,  $\text{FP}_{\text{CCM}} = 6$  and  $\text{FP}_{\text{PIR}_{\text{NNLS}}} = 2$ . The clear superiority of  $\text{PIR}_{\text{NNLS}}$  to recover the particles is emphasized with these figures, especially when high particle densities are observed (see for instance the area delimited with a white dotted line).

Then, the mean performance metrics are presented in figure 7 as a function of the particle density,  $N_{\text{ppp}}$  for the three detection methods. Averaging is performed over every  $N_{\text{ppp}}$ . The number of valid detections TP as recovered by  $\text{PIR}_{\text{NNLS}}$  remains at a very high level (actually very close to the exact amount of simulated particles), even at large particle density. This statement is emphasized by the yield values which are quasi constant and very close to 1 for all the investigated  $N_{\text{ppp}}$ . The capability of our method to recover a large amount of valid particles is further illustrated by the reliability coefficient which also remains very close to 1, for all the investigated particle densities. This result shows that, not only  $\text{PIR}_{\text{NNLS}}$  is efficient as it ‘finds’ a quasi-maximal amount of particles, but also accurate as it is not prone to produce large amount of FPs. Therefore, the improvement of the particles detection with our method is evidenced when compared to referenced algorithms in the same conditions. Indeed, DTB and CCM fail at recovering a large amount of particles when  $N_{\text{ppp}}$  is increased as illustrated by the clear drop of their yield ratio.

The high efficiency of  $\text{PIR}_{\text{NNLS}}$  is further emphasized with an insight on the mean localization errors, see figure 8(a). The  $\text{PIR}_{\text{NNLS}}$  error is always within 0.07 pixels, whatever the particle density  $N_{\text{ppp}}$  is. For comparison, at  $N_{\text{ppp}} \approx 0.09$ , the mean errors computed with  $\text{PIR}_{\text{NNLS}}$ , CCM and DTB are 0.067, 0.172 and 0.290 pixels respectively. As a conclusion, not only  $\text{PIR}_{\text{NNLS}}$  provides the best performance metrics, but it is also more accurate than the referenced methods tested in the conditions discussed in this paper.

#### 4.5. Effect of background noise

The background noise is likely to represent a large contribution to the loss of reliability of the detection algorithm. It is generally associated with non-uniform variations of grey levels in the image not related to the particle. Hence it alters

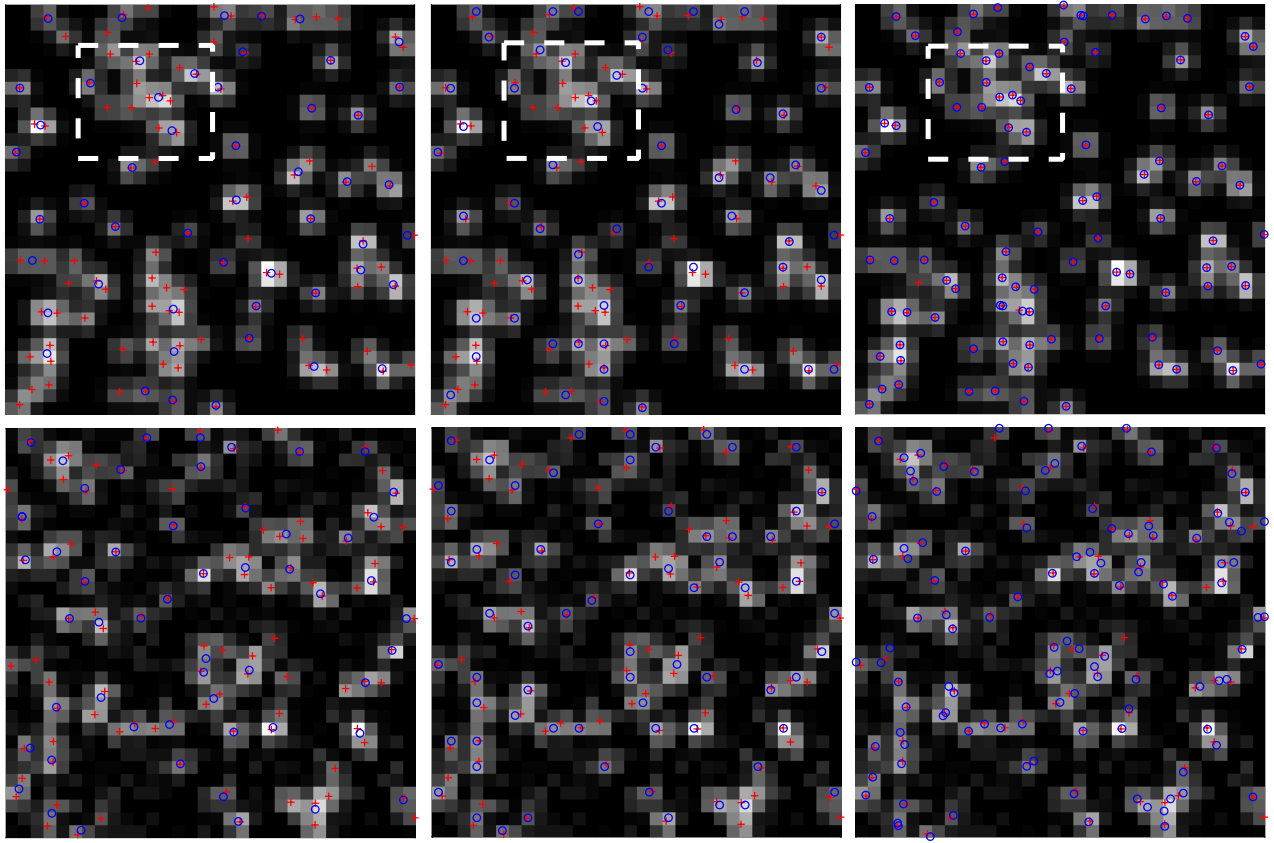


**Figure 6.** Synthetic  $32 \times 32$  pixel images on which are superimposed the localizations of the particles (red  $\times$ ) and those of the detections (blue  $\circ$ ). From left to right: CCM, DTB and  $\text{PIR}_{\text{NNLS}}$  methods. Top row: without noise; bottom row: with added noise.

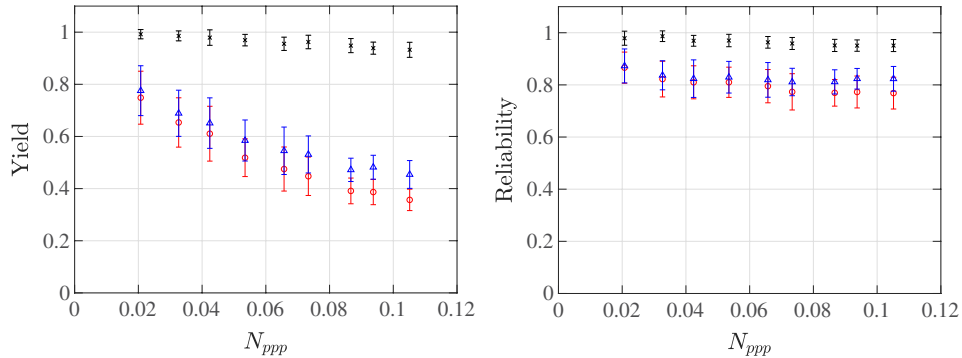


**Figure 7.** Comparison between the conventional DTB (blue  $\Delta$ ), CCM (red  $\circ$ ) and the proposed  $\text{PIR}_{\text{NNLS}}$  (black  $\times$ ) in terms of detections efficiency as a function of the particle density,  $N_{\text{ppp}}$ . Without any camera noise. Left: yield; right: reliability.

the ability of any detection method to accurately identify and localize the particles embedded in the image.

To study its impact on the performances of  $\text{PIR}_{\text{NNLS}}$ , a set of synthetic particle images is generated, with the same generation parameters as in section 4.4, except for a Gaussian noise with a zero mean value and a standard deviation  $\sigma_{\text{noise}}$  set to 5% of the 8-bit grayscale dynamic range which is added to each image. The assumed Gaussian distribution of the noise is widely used to model the thermal noise of the camera sensor. This source of noise is generally the major contribution in the PIV/PTV applications.

A representative illustration of the particle localizations as obtained with DTB, CCM and  $\text{PIR}_{\text{NNLS}}$  in the context of noisy data is presented in figure 6 (bottom row). For this particular

case with 98 generated particles, the performance metrics are:  $\text{TP}_{\text{DTB}} = 48$ ,  $\text{TP}_{\text{CCM}} = 43$  and  $\text{TP}_{\text{PIR}_{\text{NNLS}}} = 90$ ;  $\text{FP}_{\text{DTB}} = 20$ ,  $\text{FP}_{\text{CCM}} = 12$  and  $\text{FP}_{\text{PIR}_{\text{NNLS}}} = 24$ . This qualitative observation, again, illustrates the ability of  $\text{PIR}_{\text{NNLS}}$  to efficiently detect in unfavorable conditions.

The comparison of the performance metrics as obtained by the proposed  $\text{PIR}_{\text{NNLS}}$  with the conventional DTB and CCM are shown in figure 9 as a function of the particle density,  $N_{\text{ppp}}$ . Overall, for the highest tested  $N_{\text{ppp}}$ , the number of TP recovered by  $\text{PIR}_{\text{NNLS}}$  is approximately twice the one obtained with both other methods and a very small number of missed particles returned with  $\text{PIR}_{\text{NNLS}}$  leads to a yield value of 0.83. With both other detection methods, the yield values drop to approximately 0.4 for the highest particle density.

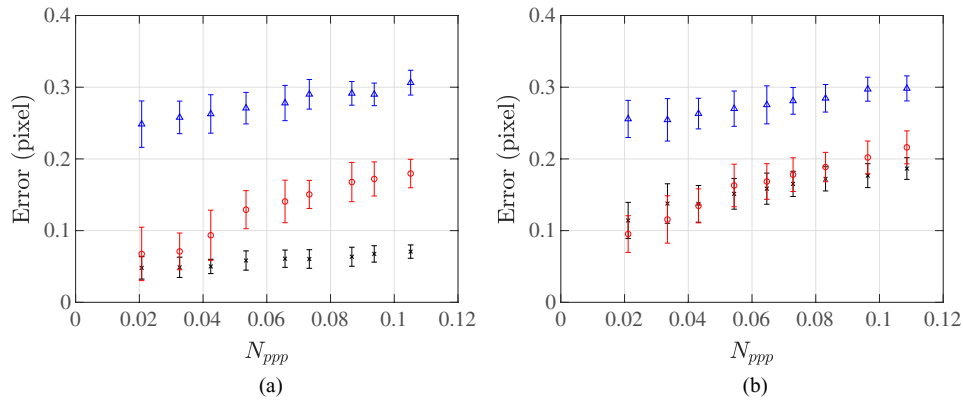


**Figure 8.** Comparison between the mean localization errors as obtained by PIR<sub>NNLS</sub> (black  $\times$ ), DTB (blue  $\triangle$ ) and CCM (red  $\circ$ ) as a function of the particle density,  $N_{ppp}$ . (a) Images without any noise. (b) Images with an added 5% Gaussian noise.

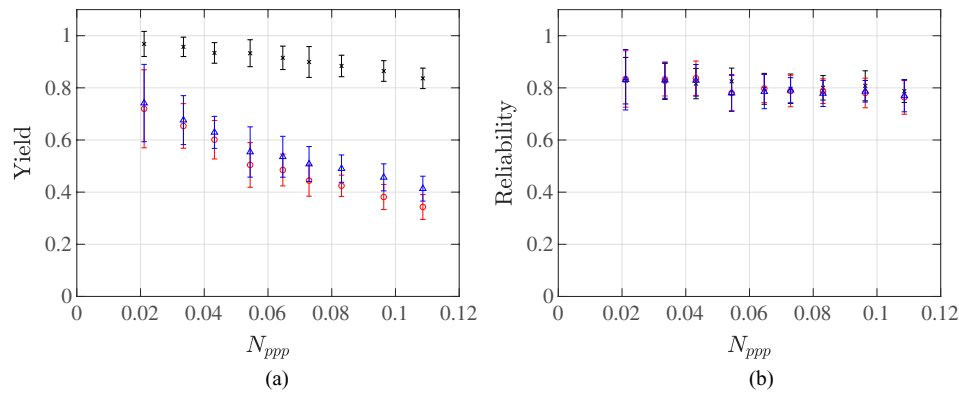


**Figure 9.** Quality of the detection as given by PIR<sub>NNLS</sub> ( $\times$ ), DTB ( $\triangle$ ) and CCM ( $\circ$ ) as a function of the particle density,  $N_{ppp}$ . With a 5% Gaussian noise. Left: yield; right: reliability.

On the other hand, the reliability coefficient exhibits similar values for each method, whatever the particle density is. This performance highlights the fact that PIR<sub>NNLS</sub> is likely to generate a larger amount of FP detections than the conventional CCM and DTB in noisy conditions. This behavior is due to the increasing mathematical difficulty to invert the present ill-posed problem (4) in the context of noisy data. This aspect requires further attention and solutions will be prospected in the future, especially for the application of this method to data collected from experiments. One of the solutions consists in performing a first treatment to the grayscale images by removal of the background noise (Mendez *et al* 2017).

The mean localization errors computed for this simulation test are shown in figure 8(b). The camera noise, as expected, increases the localization error of the PIR<sub>NNLS</sub> method when compared to the no-noise case. However, the accuracy of PIR<sub>NNLS</sub> remains comparable to the modified CCM, although the mean localization error is computed on a tremendous larger amount of TP in the case of PIR<sub>NNLS</sub> than in the case of CCM.

## 5. Implementation in large scale problems

The results presented in section 4 have demonstrated the PIR<sub>NNLS</sub> algorithm ability to detect particles over a wide

range of realistic parameters. So far, the simulation tests were carried out on  $32 \times 32$  pixel images. Meanwhile, we recall that the model matrix  $W$  to be inverted is of size  $(N, M)$ , with  $N$  the amount of selected pixels in the original image and  $M$  the amount of sub-pixels in the reconstructed sub-image, see equation (4). Hence when being confronted to larger and more realistic images, the computing time of the PIR<sub>NNLS</sub> algorithm is questionable.

The implementation of this detection method in large scale problems demands a size reduction strategy to be developed. This prior step is already embedded in the tomographic PIV framework, as for example the MLOS technique of Atkinson and Soria (2009). It consists in determining a first guess of the solution through a data selection. Restricting the possible locations of the particles thus reduces the number of columns and the overall problem size. However, the MLOS technique cannot be used in our 2D case, since we do not have several projections to confront the lines-of-sight. We propose instead to proceed with a segmentation of the original image through a local threshold procedure analogous to the conventional Otsu's method (Otsu 1979). From the segmentation procedure of the full image, blobs of contiguous pixels are obtained. Each blob contains an unknown amount of overlapping particles to be reconstructed. Therefore, the inversion procedure (sub-space definition, matrix generation, matrix inversion, local maxima detection) is performed sequentially to each blob. This modification of the method is referred as the *sequential* PIR<sub>NNLS</sub>.



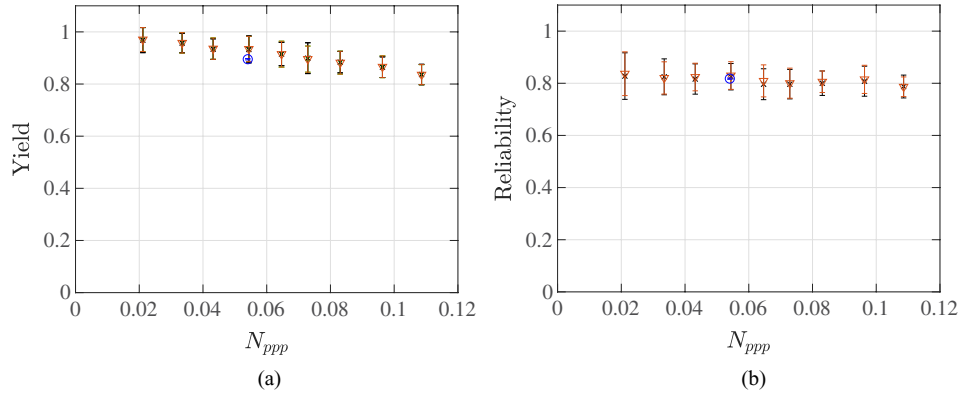


**Figure 10.** Comparison of the detection performances between the *direct* (black  $\times$ ) and the *sequential* (orange  $\nabla$ ) versions of PIR<sub>NNLS</sub> as a function of the particle density,  $N_{ppp}$  (both obtained on  $32 \times 32$  pixel images). (Blue  $\circ$ ): evaluation of the sequential PIR<sub>NNLS</sub> on large  $1024 \times 1024$  images. Left: yield; right: reliability.

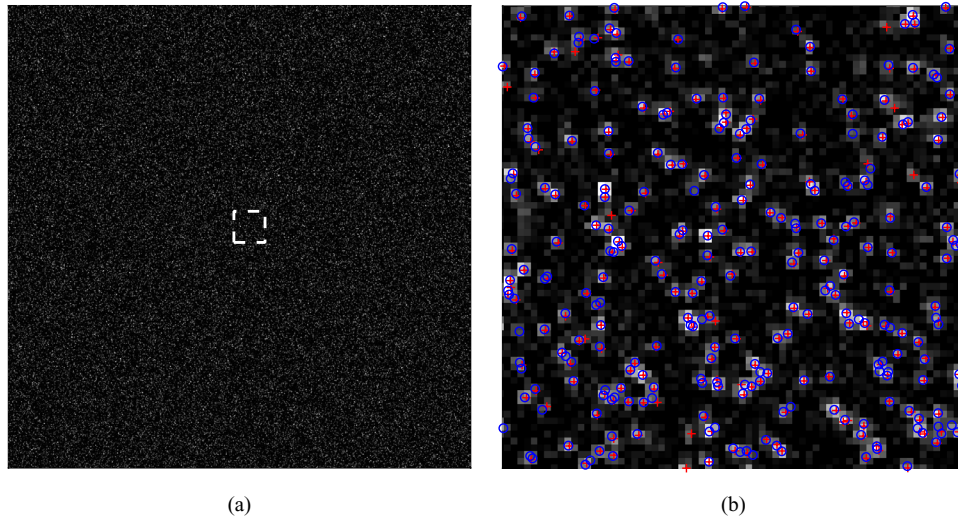


**Figure 11.** (a) Synthetic  $1024 \times 1024$  pixel images with added 5% Gaussian noise,  $N_{ppp} = 0.057$ . (b) Magnified  $70 \times 70$  pixel area. The localizations of both the particles (red  $\times$ ) and detections (blue  $\circ$ ) as processed by PIR<sub>NNLS</sub> are superimposed.

algorithm. It is to be kept in mind that the segmentation of the original image is mathematically a different problem and so, the ensemble of solutions computed over the whole domain is expected to be different as well.

### 5.1. Validation of the sequential PIR<sub>NNLS</sub> algorithm

The purpose of this section is to validate the sequential version of the PIR<sub>NNLS</sub> algorithm. To this end, the same database of synthetic  $32 \times 32$  pixel images as in section 4.5 is considered. Statistics presented below are computed from sets of 30 images. The performance metrics (yield and reliability) computed from both the *sequential* and the *direct* versions of the PIR<sub>NNLS</sub> algorithm are depicted in figure 10. Clearly, the reliability of our method to detect particles in realistic images is not affected by the sequentialization, whatever the tested particle density is. The robustness preservation of PIR<sub>NNLS</sub> is moreover obtained with a significant gain in computing time machine: for  $N_{ppp} \approx 0.05$  the sequential version of PIR<sub>NNLS</sub> is on average 5.4 times faster than its direct version, whereas for  $N_{ppp} \approx 0.1$  the benefit of the sequential version remains

of about a factor of 2.3, for computational run on the same machine. As a conclusion of this test, the sequential PIR<sub>NNLS</sub> allows a drastic reduction of computational cost without any significant reliability deterioration.

### 5.2. Application to large $1024 \times 1024$ pixels image

The *sequential* PIR<sub>NNLS</sub> algorithm is now applied to large  $1024 \times 1024$  pixel images with a 5% Gaussian noise. Figure 11(a) displays one noisy  $1024 \times 1024$  pixel image with a particle images density of  $N_{ppp} = 0.057$ . To better appreciate the particle identification and localization performance, a magnified area of  $70 \times 70$  pixel extend (delimited by the white dashed-line) is represented in figure 11(b) on which the particles and detections positions are superimposed.

The performances obtained by the *sequential* PIR<sub>NNLS</sub> on this particular set of large images are shown in figure 10 for comparison with those obtained with the  $32 \times 32$  pixel images. Although a slight decrease is observed in terms of recovered particles, the reliability of PIR<sub>NNLS</sub> is unchanged, whatever the investigated  $N_{ppp}$  is.

## 6. Conclusion

A novel algorithm for the identification and localization of particle images in PTV was proposed. The approach presented is based on the particle position reconstruction problem through the inversion of a linear model connecting the PTV signal with a particle-based representation of the 3D-to-2D projection. The size of the point spread function (PSF), defined as a 2D Gaussian intensity distribution in this work, is the only input parameter to be *a priori* estimated.

As a preliminary study, performance tests were conducted with synthetically generated particle images and against a large exploration of the generating conditions (particle density, PSF size, background noise). The obtained results showed that the inversion procedure promotes not only the non-negativity but also the sparsity of the sought solution. This intrinsic characteristic of our method ensures good performances when identifying and localizing particles in severely overlapped particle image fields. A slight decrease in reliability was observed when increasing the standard deviation of the background noise. This aspect requires further attention and work is in progress along these lines.

Overall, the proposed technique is robust in noisy conditions, and the comparison with other conventional detection techniques demonstrated its ability to reliably localize more particles out of a dense particle image field.

The attractive properties of  $\text{PIR}_{\text{NNLS}}$ , *a priori* specifically designed for 2D-PTV, are likely to bring further insight in a variety 3D-flow measurements. While hybrid tomographic-PTV methods, for example, are becoming more popular (Schanz *et al* 2016) with their relevant 2D particle identification issue (Wieneke 2013, Ben Salah *et al* 2018), we believe that  $\text{PIR}_{\text{NNLS}}$  is likely to increase the reachable particle density of such techniques.

## ORCID iDs

Jean-François Krawczynski  <https://orcid.org/0000-0001-9661-4688>

## References

- Adrian R J 1984 Scattering particle characteristics and their effect on pulsed laser measurements of fluid flow: speckle velocimetry versus particle image velocimetry *Appl. Opt.* **23** 1690
- Angarita-Jaimes N C, Roca M G, Towers C E, Read N D and Towers D P 2009 Algorithms for the automated analysis of cellular dynamics within living fungal colonies *J. Cytometry A* **75** 768–80
- Atkinson C and Soria J 2009 An efficient simultaneous reconstruction technique for tomographic particle image velocimetry *Exp. Fluids* **47** 553–68
- Ben Salah R, Alata O, Tremblais B, Thomas L and David L 2018 Tomographic reconstruction of 3D objects using marked point process framework *J. Math. Imaging Vis.* **60** 1132–49
- Brady M R, Raben S G and Vlachos P P 2009 Methods for digital particle image sizing (DPIS): comparisons and improvements *Flow Meas. Instrum.* **20** 207–19
- Cardwell N D, Vlachos P P and Thole K A 2011 A multiparametric particle-pairing algorithm for particle tracking in single and multiphase flows *Meas. Sci. Technol.* **22** 105406
- Champagnat F, Cornic P, Cheminet A, Leclaire B and Le Besnerais G 2014 Tomographic PIV: particles versus blobs *Meas. Sci. Technol.* **25** 084002
- Cowen E A and Monismith S G 1997 A hybrid digital particle tracking velocimetry technique *Exp. Fluids* **22** 199–211
- Elsinga G E, Scarano F, Wieneke B and van Oudheusden B 2006 Tomographic particle image velocimetry *Exp. Fluids* **41** 933–47
- Feng Y, Goree J and Liu B 2011 Errors in particle tracking velocimetry with high-speed cameras *Rev. Sci. Instrum.* **82** 053707
- Jemec J, Pernuš F, Likar B and Bürmen M 2017 2D Sub-pixel point spread function measurement using a virtual point-like source *Int. J. Comput. Vis.* **121** 391–402
- Kahler C J, Scharnowski S and Cierpka C 2012 On the uncertainty of digital PIV and PTV near walls *Exp. Fluids* **52** 1641–56
- Krawczynski J F, Renou B and Danaila L 2010 The structure of the velocity field in a confined flow driven by an array of opposed jets *Phys. Fluids* **22** 045104
- Lawson C L and Hanson R J 1974 *Solving Least-Squares Problems* vol 15 (Upper Saddle River, NJ: Prentice-Hall) ch 23 p 161
- Lecordier B and Westerweel J 2004 The EUROPIV synthetic image generator (SIG) *Particle Image Velocimetry: Recent Improvements* vol 15 (Berlin: Springer) ch 23 pp 145–61
- Lei Y C, Tien W H, Duncan J, Paul M, Ponchaut N, Mouton C, Dabiri D, Rosgen T and Hove J 2012 A vision-based hybrid particle tracking velocimetry (PTV) technique using a modified cascade correlation peak-finding method *Exp. Fluids* **53** 1251–68
- Marxen M, Sullivan P E, Loewen M R and Jähne B 2000 Comparison of Gaussian particle center estimators and the achievable measurement density for particle tracking velocimetry *Exp. Fluids* **29** 145–53
- Mendez M A, Raiola M, Masullo A, Discetti S, Ianiro A, Theunissen R and Buchlin J M 2017 POD-based background removal for particle image velocimetry *Exp. Therm. Fluid Sci.* **80** 181–92
- Mikheev A V and Zubtsov V M 2008 Enhanced particle-tracking velocimetry (EPTV) with a combined two-component pair-matching algorithm *Meas. Sci. Technol.* **19** 085401
- Nogueira J, Lecuona A and Rodriguez R A 2005 Limits on the resolution of correlation PIV iterative methods. Fundamentals *Exp. Fluids* **39** 305–13
- Ohmi K and Li H Y 2000 Particle-tracking velocimetry with new algorithms *Meas. Sci. Technol.* **11** 603–16
- Otsu N 1979 A threshold selection method from gray-level histograms *IEEE Trans. Syst. Man Cybern.* **9** 62–6
- Petra S, Schnörr C, Schröder A and Wieneke B 2007 Tomographic image reconstruction in experimental fluid dynamics: synopsis and problems *Proc. 6th Workshop on Modelling of Environmental and Life Sciences Problems* (Ed. Acad. Romane, Bucuresti, Constanta, Romania)
- Raffel M, Willert C E, Wereley S T and Kompenhans J 2007 *Particle Image Velocimetry: a Practical Guide* (Berlin: Springer)
- Reichenbach S E, Park S K and Narayanswamy R 1991 Characterizing digital image acquisition devices *Opt. Eng.* **30** 170–7
- Ruhnau P, Guetter C, Putze T and Schnörr C 2005 A variational approach for particle tracking velocimetry *Meas. Sci. Technol.* **16** 1449–58
- Saarenrinne P and Piirto M 2000 Turbulent kinetic energy dissipation rate estimate from PIV velocity vector fields *Exp. Fluids* **29** 300–7
- Scarano F 2003 Theory of non-isotropic spatial resolution in PIV *Exp. Fluids* **35** 268–77

- Schanz D, Gesemann S, Schröder A, Wieneke B and Novara M 2013 Non-uniform optical transfer functions in particle imaging: calibration and application to tomographic reconstruction *Meas. Sci. Technol.* **24** 1–15
- Schanz D, Gesemann S and Schröder A 2016 Shake-The-Box: Lagrangian particle tracking at high particle image densities *Exp. Fluids* **57** 70
- Takehara K and Etoh T 1999 A study on particle identification in PTV particle mask correlation method *J. Vis.* **1** 313–23
- Tanaka T and Eaton J K 2007 A correction method for measuring turbulence kinetic energy dissipation rate by PIV *Exp. Fluids* **42** 893–902
- Wieneke B 2013 Iterative reconstruction of volumetric particle distribution *Meas. Sci. Technol.* **24** 024008